

Research Paper

A flexible mixed-order formula for tetrahedron elements based on SBFEM

Kai Chen^{a,b}, Degao Zou^{a,b,*}, Guoyang Yi^{a,b}, Xiupeng Nie^{a,b}, Yongqian Qu^{a,b}^a The State Key Laboratory of Coastal and Offshore Engineering, Dalian University of Technology, Dalian, Liaoning 116024, China^b School of Hydraulic Engineering, Dalian University of Technology, Dalian, Liaoning 116024, China

ARTICLE INFO

Keywords:

Scaled boundary finite element method

Tetrahedron discretization

Mixed-order interpolation

ABSTRACT

The tetrahedrons offer advantages in terms of its adaptability to complex geometries and high-efficiency of automated discretization. However, the performance is greatly limited by the weak accuracy suffered from first-order elements, as well as the significant computational burden required for quadratic cells. In this paper, a flexible mixed-order tetrahedron element is constructed on the basis of SBFEM theory, specifically, a formula for the interpolation of circumferential boundary is developed with the union of quadratic and first-order seamlessly, benefiting the combination of triangle area coordinates and the line drawing approach. Additionally, a flexural angle index of tetrahedral edges and regional customization are proposed as the modification method for determining order conversion. Subsequently, the accuracy of the proposed method in addressing various issues is investigated. The results show that the performance of tetrahedrons is satisfactorily enhanced through the utilization of 64 distinct order combination modes; and compared with its quadratic form, the calculation workload has been effectively decreased with no loss of accuracy. In summary, the analytical performance of tetrahedrons can be enhanced reasonably, which provides an effective approach for rapid and accurate analysis for critical structures.

1. Introduction

Mesh discretization is a fundamental aspect of finite element numerical simulation, and the rationality and computing efficiency of the simulation are directly determined by the quality and density of mesh. Currently, the most frequently utilized 3D mesh types include hexahedron and tetrahedron, with the hexahedron mesh offering high solving accuracy, but lacking in complex geometric adaptability; Besides, the well-developed tetrahedral mesh exhibits remarkable adaptability to intricate structures. However, its first-order form has a relatively lower calculation accuracy, and a great many meshes are required to meet the accuracy requirements for refined analysis, resulting in a substantial computational load. On the other hand, quadratic tetrahedral elements exhibit high accuracy, but it comes with a significant increase in degrees of freedom, making the calculations relatively time-consuming.

With the continuous improvement of computational power and solving ability, numerical simulation is gradually advancing towards greater refinement and striving to reflect the geometrical characteristics of structures with high fidelity. This necessitates higher requirements for the universality of mesh discretization algorithms. Due to its superior universality, tetrahedron element has become a primary selection

among scholars, such as the high-efficient tetrahedral discretization algorithm (Davide et al., 2021); the analysis of synaptic transmission in biological structures (Maciej, 2023). The inversion analysis of the geomagnetic field (Rong et al., 2022), the application of high order positivity-preserving conservative (Nuo et al., 2022), and other fields (Areias et al., 2022; Schneider et al., 2022; Meneghetti et al., 2018; Xue et al., 2022; Baiges et al., 2020) has been promoted and applied. Overall, it is difficult to achieve the coexistence of high accuracy and efficiency using tetrahedron for practical applications, which greatly hindered the promotion and application of this grids.

Efficient optimization of accuracy and effectiveness can be achieved through the application of mixed-order elements, employing high-precision quadratic element simulation for crucial positions while efficient first-order element for other computational domains. In this manner, the constraints of tetrahedral elements can be effectively mitigated. Currently, the mixed-order method can be implemented via two approaches, which is stated as follows:

This technique starts with the use of “Serendipity elements” and introduces the concept of mapping transformation, which necessitates a mapping relationship between the element in the physical domain and the parent element. Therefore, nodes that are situated on the boundaries

* Corresponding author at: The State Key Laboratory of Coastal and Offshore Engineering, Dalian University of Technology, Dalian, Liaoning 116024, China.
E-mail address: zoudegao@dlut.edu.cn (D. Zou).

of elements inside the physical domain must be mapped in a manner that is consistent with the parent element. However, mapping distortion in nodes may occur during this process (Utku, 1999). Researchers have suggested a more adaptable parent element with movable edge node locations to address this problem (Wriggers et al., 2021). Nevertheless, the implementation of this approach is inconvenient, and its simplicity could be further optimized.

Secondly, the scaled boundary finite element technique (SBFEM), which is a semi-analytical approach developed by Wolf and Song (Song and Wolf, 1997, 2009, 2018), may be used to implement the mixed-order elements. SBFEM offers the advantage of dimensionality reduction via circumferential numerical analysis and radial analytical analysis, it is evident that the formulation for mixed-order elements can be automatically fulfilled. Specifically, each boundary element can be interpolated through the cells with varying orders without any unnecessary modifications or increasing the difficulty of numerical integration, and it has currently been applied to the automatic analysis (Saputra et al., 2017) and mechanical analysis of planar solids (Chen et al., 2023). Furthermore, many advantages can be revealed, including the simplicity for formulating the polygonal/polyhedron elements, solution of infinite domain problem and stress singular problem, and name a few. And after many years of development, SBFEM has garnered extensive attention from researchers, some representative works can be referred. Ye and Zang et al. (Ye et al., 2023; Zang et al., 2023) developed a novel algorithm combined isogeometric analysis and SBFEM for piezoelectric laminated and cylindrical shells. Du and Shen et al. (Du et al., 2023; Shen et al., 2024) utilized SBFEM to address the challenges of static and dynamic crack initiation and propagation, offering a more precise depiction of local cracking damage zones. Soil-structure interaction analysis is a pervasive and challenging problem in geotechnical engineering (Gao et al., 2023a, 2023b). Zhang and Zhao et al. (Zhang et al., 2022, 2023; Zhao et al., 2023) proposed a flexible structural dynamic analysis methods based on SBFEM and engineering application is achieved. Zhang et al. (Zhang et al., 2016, 2020) makes SBFEM extended to topology optimization problems, wherein satisfactory improvements in computational efficiency and simplification are revealed. Researchers have also conducted SBFEM research in various fields, including the application of nonlinear analysis in complex geotechnical engineering (Chen et al., 2017; Chen et al., 2018a), 2D Cosserat continuum analysis (Chen et al., 2021), slope stability analysis (Nie et al., 2022), wave propagation problems (Zhang et al., 2023a, 2024), structural damage analysis (Qu et al., 2020; Zhang et al., 2018, 2019; Yu et al., 2023), and bending and vibration analyses of structures (Zhang et al., 2023b; Liu et al., 2021a, 2021b).

In order to enhance the numerical performance of tetrahedral elements, a flexible mixed-order tetrahedron is presented based on SBFEM, wherein quadratic elements and first-order elements can be united seamlessly, with the help of combining the triangle area coordinates and the line drawing approach to formula the circumferential interpolation function. Additionally, an order conversion criterion based on the deformation curvature of each edge located on the tetrahedron is also proposed. Finally, the accuracy and efficiency of the proposed method for various problems are investigated through several numerical examples.

2. SBFEM Formula for tetrahedron cross-order elements

2.1. Circumferential interpolation

Obvious to all, SBFEM has been studied and adopted by academia for decades, and a large amount of academia literatures are available for reference. In order to improve the brevity and readability of the paper, the theoretical demonstration of the proposed method is introduced through the main equations in this section. A typical tetrahedron element in the SBFEM coordinates is displayed in Fig. 1.

Triangular elements can be used to discretize the boundary in the

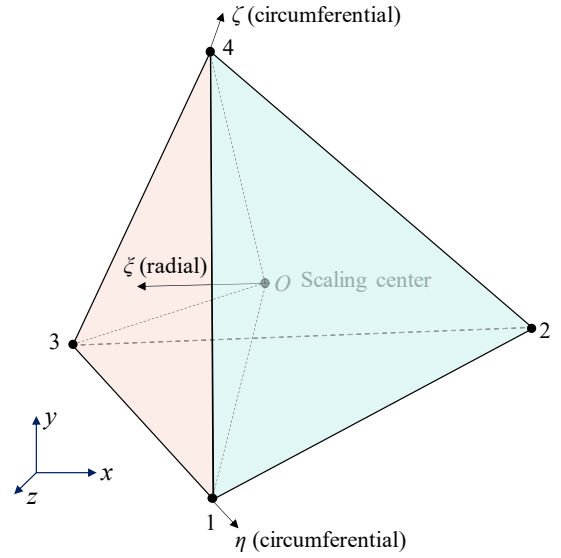


Fig. 1. Typical tetrahedron element of scaled boundary finite element method.

circumferential direction, where the first-order or quadratic interpolation can be employed according to demands, and a local coordinate system (η, ζ) similar to FEM is adopted. Meanwhile, a radial coordinate ξ is defined, whose value is 0 at the scale center O while 1.0 at the boundary.

2.1.1. Interpolation function based on area coordinates

(1) area coordinates

The defining diagram for the area coordinates is shown in Fig. 2, where 1, 2, and 3 represent the three counterclockwise ordered vertices of a triangle. According to the Cartesian coordinates of the three vertices denoted as (x_1, y_1) , (x_2, y_2) and (x_3, y_3) , the triangle area can be expressed as

$$A = \frac{1}{2} \begin{vmatrix} 1 & x_1 & y_1 \\ 1 & x_2 & y_2 \\ 1 & x_3 & y_3 \end{vmatrix} = \frac{1}{2} ((x_2 - x_1)(y_3 - y_1) - (x_3 - x_1)(y_2 - y_1)) \quad (1)$$

And a point $P(x, y)$ inside the triangle is selected, then the triangle can be divided into three sub-triangles via three lines connecting P with the vertices. By replacing the coordinates of vertex 1 of the triangle (x_1, y_1) with the coordinates of point $P(x, y)$, the area of the sub-triangle $P23$ calculated from the equation (1) is expressed as

$$A_{P23} = \frac{1}{2} ((x_2 - x)(y_3 - y) - (x_3 - x)(y_2 - y)) \quad (2)$$

Similarly, the areas of the sub-triangles $P31$ and $P12$ are equal to

$$A_{P31} = \frac{1}{2} ((x_3 - x)(y_1 - y) - (x_1 - x)(y_3 - y)) \quad (3)$$

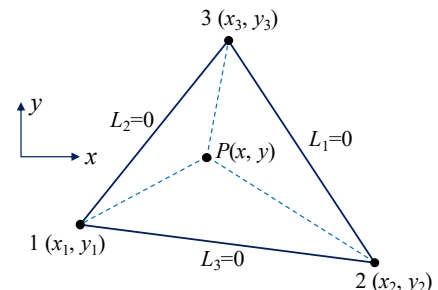


Fig. 2. Area coordinates L_1, L_2, L_3 in a triangle.

$$A_{P12} = \frac{1}{2}((x_1 - x)(y_2 - y) - (x_2 - x)(y_1 - y)) \quad (4)$$

The area coordinates L_1, L_2, L_3 are defined as the ratios of the areas of the sub-triangles to the area of the whole triangle, which can be expressed as:

$$L_1 = \frac{A_{P23}}{A}; L_2 = \frac{A_{P31}}{A}; L_3 = \frac{A_{P12}}{A} \quad (5)$$

As can be seen from Fig. 2, the area coordinate L_i ($i = 1, 2, 3$) is equal to 1 at node i while 0 on the opposite edge of the point. For example, the area coordinate L_1 is equal to 1 at node 1, yet to 0 on side $\overline{23}$.

(2) Interpolation function

Interpolation can be used to obtain the coordinates of points on line elements, as demonstrated in Eqs. (6) and (7).

$$\mathbf{x}_b(\eta, \zeta) = \mathbf{N}(\eta, \zeta)\mathbf{x}_b \quad (6)$$

$$\mathbf{y}_b(\eta, \zeta) = \mathbf{N}(\eta, \zeta)\mathbf{y}_b \quad (7)$$

$$\mathbf{N}(\eta, \zeta) = [N_1(\eta, \zeta), N_2(\eta, \zeta), N_3(\eta, \zeta), \dots, N_m(\eta, \zeta)] \quad (8)$$

$$N_1(\zeta, \eta) = 1 - \zeta - \eta, N_2(\zeta, \eta) = \eta, N_3(\zeta, \eta) = \zeta \quad (9)$$

$$N_1(\zeta, \eta) = (1 - \zeta - \eta)(1 - \zeta - 2\eta), N_2(\zeta, \eta) = \eta(2\eta - 1), N_3(\zeta, \eta) = \zeta \\ N_4(\zeta, \eta) = 4(1 - \zeta - \eta)\eta \quad (10)$$

$$N_1(\zeta, \eta) = (1 - \zeta - \eta)(1 - \zeta - 2\eta), N_2(\zeta, \eta) = \eta(2\eta - 1), N_3(\zeta, \eta) = \zeta \\ N_4(\zeta, \eta) = 4(1 - \zeta - \eta)\eta, N_5(\zeta, \eta) = 4\eta\zeta \quad (11)$$

$$N_1(\zeta, \eta) = (1 - \zeta - \eta)(1 - \zeta - 2\eta), N_2(\zeta, \eta) = \eta(2\eta - 1), N_3(\zeta, \eta) = \zeta \\ N_4(\zeta, \eta) = 4(1 - \zeta - \eta)\eta, N_5(\zeta, \eta) = 4\eta\zeta, N_6(\zeta, \eta) = 4(1 - \zeta - \eta)\zeta \quad (12)$$

where $\mathbf{N}(\eta, \zeta)$ is the shape function of the surface element with m nodes, which has shown in Eq. (8). Here, four interpolation modes, including first-order, mixed-order, and quadratic elements, with their respective expressions presented in Eq. (9) to (12), are applied. Additionally, a diagram demonstrating the process is displayed in Fig. 3, wherein the first-order equation (9) corresponding to Scheme A, moreover, Scheme B and Scheme C are the mixed-order interpolation, can be derived as equation (10) and (11), respectively. Quadratic element is demonstrated

as Scheme D, and formulated in equation (12). Due to the advantage of boundary discretization of SBFEM, the boundary elements with mixed orders can be smoothly derived and implemented within this theoretical framework. Based on boundary area coordinates, the point in the Cartesian coordinate $\{x, y\}$ within the 3D domain can be represented in the scaled boundary coordinates (ξ, η, ζ) using the relation:

$$\mathbf{x}(\xi, \eta, \zeta) = \xi \mathbf{N}(\eta, \zeta) \mathbf{x}_b \quad (13)$$

$$\mathbf{y}(\xi, \eta, \zeta) = \xi \mathbf{N}(\eta, \zeta) \mathbf{y}_b \quad (14)$$

2.1.2. Formula of radial solution

In the theory of scaled boundary finite element method, a radial displacement function $\mathbf{u}(\xi)$ is introduced, in this case, the displacement of a point in the tetrahedral domain formed by connecting the scaling center and the vertices of triangular surface can be expressed by the radial displacement function, as shown in Eq. (15).

$$\mathbf{u}(\xi, \eta, \zeta) = \mathbf{N}_u(\eta, \zeta) \mathbf{u}(\xi) \quad (15)$$

in which $\mathbf{N}_u(\eta, \zeta)$ is the interpolation function of the triangle surface element. Following the principle of virtual work, the SBFEM displacement equation with respect to $\mathbf{u}(\xi)$ can be formed, which is expressed in Eq. (16).

$$E_0 \xi^2 \mathbf{u}(\xi)_{,\xi\xi} + (2E_0 - E_1 + E_1^T) \xi \mathbf{u}(\xi)_{,\xi} + (E_1^T - E_2) \mathbf{u}(\xi) + \mathbf{F}(\xi) = 0 \quad (16)$$

As it can be seen that Eq. (16) describes the equilibrium condition in the ξ direction, in which E_i ($i = 0, 1, 2$) are coefficient matrices that depend on the geometry and material properties, and they are defined as follows:

$$E_0 = \int_{-1}^1 \int_{-1}^1 \mathbf{B}_1^T(\eta, \zeta) \mathbf{D} \mathbf{B}_1(\eta, \zeta) |\mathbf{J}(\eta, \zeta)| d\eta d\zeta \quad (17a)$$

$$E_1 = \int_{-1}^1 \int_{-1}^1 \mathbf{B}_2^T(\eta, \zeta) \mathbf{D} \mathbf{B}_1(\eta, \zeta) |\mathbf{J}(\eta, \zeta)| d\eta d\zeta \quad (17b)$$

$$E_2 = \int_{-1}^1 \int_{-1}^1 \mathbf{B}_2^T(\eta, \zeta) \mathbf{D} \mathbf{B}_2(\eta, \zeta) |\mathbf{J}(\eta, \zeta)| d\eta d\zeta \quad (17c)$$

where \mathbf{D} is the elastic matrix, and $|\mathbf{J}(\eta, \zeta)|$ represents the Jacobian matrix determinant. $\mathbf{B}_1(\eta, \zeta)$ and $\mathbf{B}_2(\eta, \zeta)$ mean the strain displacement

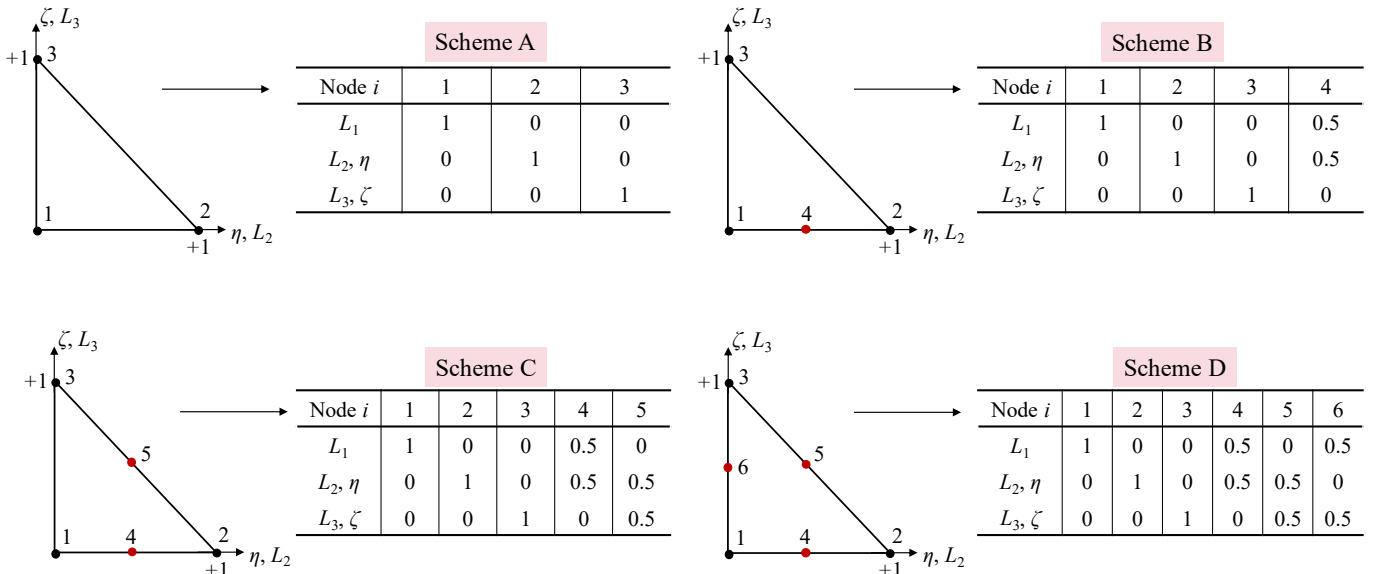


Fig. 3. Illustration of the triangular shaped function.

transformation matrices, which can be written as follows:

$$\mathbf{B}_1(\eta, \zeta) = \mathbf{b}_1(\eta, \zeta) \mathbf{N}_u(\eta, \zeta) \quad (18a)$$

$$\mathbf{B}_2(\eta, \zeta) = \mathbf{b}_2(\eta, \zeta) \mathbf{N}_u(\eta, \zeta) + \mathbf{b}_3(\eta, \zeta) \mathbf{N}_u(\eta, \zeta)_{,\zeta} \quad (18b)$$

$$\mathbf{b}_1(\eta, \zeta) = \frac{1}{|J|} \begin{bmatrix} \mathbf{y}_{,\eta} \mathbf{z}_{,\zeta} - \mathbf{z}_{,\eta} \mathbf{y}_{,\zeta} & 0 & 0 \\ 0 & \mathbf{z}_{,\eta} \mathbf{x}_{,\zeta} - \mathbf{x}_{,\eta} \mathbf{z}_{,\zeta} & 0 \\ 0 & 0 & \mathbf{x}_{,\eta} \mathbf{y}_{,\zeta} - \mathbf{y}_{,\eta} \mathbf{x}_{,\zeta} \\ 0 & \mathbf{x}_{,\eta} \mathbf{y}_{,\zeta} - \mathbf{y}_{,\eta} \mathbf{x}_{,\zeta} & \mathbf{z}_{,\eta} \mathbf{x}_{,\zeta} - \mathbf{x}_{,\eta} \mathbf{z}_{,\zeta} \\ \mathbf{x}_{,\eta} \mathbf{y}_{,\zeta} - \mathbf{y}_{,\eta} \mathbf{x}_{,\zeta} & 0 & \mathbf{y}_{,\eta} \mathbf{z}_{,\zeta} - \mathbf{z}_{,\eta} \mathbf{y}_{,\zeta} \\ \mathbf{z}_{,\eta} \mathbf{x}_{,\zeta} - \mathbf{x}_{,\eta} \mathbf{z}_{,\zeta} & \mathbf{y}_{,\eta} \mathbf{z}_{,\zeta} - \mathbf{z}_{,\eta} \mathbf{y}_{,\zeta} & 0 \end{bmatrix} \quad (19a)$$

$$\mathbf{b}_2(\eta, \zeta) = \frac{1}{|J|} \begin{bmatrix} \mathbf{z} \mathbf{y}_{,\zeta} - \mathbf{y} \mathbf{z}_{,\zeta} & 0 & 0 \\ 0 & \mathbf{x} \mathbf{z}_{,\zeta} - \mathbf{z} \mathbf{x}_{,\zeta} & 0 \\ 0 & 0 & \mathbf{y} \mathbf{x}_{,\zeta} - \mathbf{x} \mathbf{y}_{,\zeta} \\ 0 & \mathbf{y} \mathbf{x}_{,\zeta} - \mathbf{x} \mathbf{y}_{,\zeta} & \mathbf{x} \mathbf{z}_{,\zeta} - \mathbf{z} \mathbf{x}_{,\zeta} \\ \mathbf{y} \mathbf{x}_{,\zeta} - \mathbf{x} \mathbf{y}_{,\zeta} & 0 & \mathbf{z} \mathbf{y}_{,\zeta} - \mathbf{y} \mathbf{z}_{,\zeta} \\ \mathbf{x} \mathbf{z}_{,\zeta} - \mathbf{z} \mathbf{x}_{,\zeta} & \mathbf{z} \mathbf{y}_{,\zeta} - \mathbf{y} \mathbf{z}_{,\zeta} & 0 \end{bmatrix} \quad (19b)$$

$$\mathbf{b}_3(\eta, \zeta) = \frac{1}{|J|} \begin{bmatrix} \mathbf{y} \mathbf{z}_{,\eta} - \mathbf{z} \mathbf{y}_{,\eta} & 0 & 0 \\ 0 & \mathbf{z} \mathbf{x}_{,\eta} - \mathbf{x} \mathbf{z}_{,\eta} & 0 \\ 0 & 0 & \mathbf{x} \mathbf{y}_{,\eta} - \mathbf{y} \mathbf{x}_{,\eta} \\ 0 & \mathbf{x} \mathbf{y}_{,\eta} - \mathbf{y} \mathbf{x}_{,\eta} & \mathbf{z} \mathbf{x}_{,\eta} - \mathbf{x} \mathbf{z}_{,\eta} \\ \mathbf{x} \mathbf{y}_{,\eta} - \mathbf{y} \mathbf{x}_{,\eta} & 0 & \mathbf{y} \mathbf{z}_{,\eta} - \mathbf{z} \mathbf{y}_{,\eta} \\ \mathbf{z} \mathbf{x}_{,\eta} - \mathbf{x} \mathbf{z}_{,\eta} & \mathbf{y} \mathbf{z}_{,\eta} - \mathbf{z} \mathbf{y}_{,\eta} & 0 \end{bmatrix} \quad (19c)$$

$\mathbf{F}(\xi)$ in Eq. (16) is the external load vector, in the case of $\mathbf{F}(\xi) = 0$, the equilibrium equation can be changed into a second-order homogeneous partial differential equation, in this manner, if a variable $\mathbf{X}(\xi)$ is introduced, whose formula is given in Eq. (20), the differential equation can be re-written as the form in Eq. (21).

$$\mathbf{X}(\xi) = \begin{Bmatrix} \mathbf{u}(\xi) \\ \mathbf{q}(\xi) \end{Bmatrix} \quad (20)$$

$$\xi \mathbf{X}(\xi)_{,\xi} = -\mathbf{Z} \mathbf{X}(\xi) \quad (21)$$

where \mathbf{Z} means the Hamiltonian matrix, and its expression is offered in Eq. (22), $\mathbf{q}(\xi)$ is the internal nodal force function along the radial lines.

$$\mathbf{Z} = \begin{bmatrix} \mathbf{E}_0^{-1} \mathbf{E}_1^T & -\mathbf{E}_0^{-1} \\ \mathbf{E}_1 \mathbf{E}_0^{-1} \mathbf{E}_1^T - \mathbf{E}_2 & -\mathbf{E}_1 \mathbf{E}_0^{-1} \end{bmatrix} \quad (22)$$

The Hamiltonian matrix \mathbf{Z} can be decoupled by the eigenvalue decomposition process, and the relationship formula for the tetrahedron element can be expressed as

$$\mathbf{Z} \begin{bmatrix} \boldsymbol{\psi}_u \\ \boldsymbol{\psi}_q \end{bmatrix} = \begin{bmatrix} \boldsymbol{\psi}_u \\ \boldsymbol{\psi}_q \end{bmatrix} \mathbf{S}_n \quad (23)$$

where \mathbf{S}_n is a diagonal matrix with the elements in the diagonal corresponding to the eigenvalues, $\boldsymbol{\psi}_u$ and $\boldsymbol{\psi}_q$ are transformation matrices corresponding to the modal displacements and forces, respectively.

The general solutions for the $\mathbf{u}(\xi)$ and $\mathbf{q}(\xi)$ are expressed as:

$$\begin{aligned} \mathbf{u}(\xi) &= \boldsymbol{\psi}_u \xi^{-S_n} \mathbf{c}_n \\ \mathbf{q}(\xi) &= \boldsymbol{\psi}_q \xi^{-S_n} \mathbf{c}_n \end{aligned} \quad (24)$$

where the integration constants \mathbf{c}_n is determined by the nodal displacements on the boundary $u_b = u(\xi = 1)$, which can be written as Eq. (25). Further, the shape function $\Phi(\xi, \eta, \zeta)$ in the tetrahedron can be derived, which can be expressed in Eq. (26).

$$\mathbf{c}_n = \boldsymbol{\psi}_u^{-1} \mathbf{u}_b \quad (25)$$

$$\Phi(\xi, \eta, \zeta) = \mathbf{N}_u(\eta, \zeta) \boldsymbol{\psi}_u \xi^{-S_n} \boldsymbol{\psi}_u^{-1} \quad (26)$$

The strain expression Eq. (27a) has been given in the book of SBFEM (Wolf and Song 2003, 2018), therefore, the strain-displacement

transformation matrix $\mathbf{B}(\xi, \eta, \zeta)$ can be extracted from Eq. (27b), which is shown in Eq. (27c).

$$\boldsymbol{\varepsilon}(\xi, \eta, \zeta) = \mathbf{B}_1(\eta, \zeta) \mathbf{u}(\xi)_{,\xi} + \xi^{-1} \mathbf{B}_2(\eta, \zeta) \mathbf{u}(\xi) \quad (27a)$$

$$\boldsymbol{\varepsilon}(\xi, \eta, \zeta) = [\mathbf{B}_1(\eta, \zeta) \boldsymbol{\psi}_u [-\mathbf{S}_n] + \mathbf{B}_2(\eta, \zeta) \boldsymbol{\psi}_u] \xi^{-S_n-1} \boldsymbol{\psi}_u^{-1} \mathbf{u}_b \quad (27b)$$

$$\mathbf{B}(\xi, \eta, \zeta) = [\mathbf{B}_1(\eta, \zeta) \boldsymbol{\psi}_u [-\mathbf{S}_n] + \mathbf{B}_2(\eta, \zeta) \boldsymbol{\psi}_u] \xi^{-S_n-1} \boldsymbol{\psi}_u^{-1} \quad (27c)$$

2.2. Integration within the tetrahedron

In order to be usable for elastic-plastic analysis, the chunked intra-domain integration scheme is adopted in this paper, which is proposed previously by Sukumar and Tabarraei (2004), and Hammer's integration rule is employed to determine the location of Gaussian points in the domain of the tetrahedral cells. In this method, the element is separated into four sub-tetrahedron elements by connecting the scaling center O and the vertices of triangular surface boundary. A representative tetrahedron is illustrated in Fig. 4, which can be divided into four sub-tetrahedrons. For each sub-tetrahedral element, the integral is integrated separately, and then the integral of the tetrahedral element is obtained by assembling the 4 sub-tetrahedrons in blocks.

According to Hammer integration rule in the tetrahedron, the linear and quadratic integration schemes, which contain one and four integration points respectively, are adopted in the tetrahedron element, and their integration point coordinates and weights are listed in Table 1. Depending on the node numbers of the surface triangular element, two types of integration point schemes can be employed to integrate mixed-order tetrahedron element.

Based on the SBFEM theory and interpolation function, volume coordinates of the four integration points can be converted into local coordinates (L_1, L_2, L_3, ξ), and the corresponding coordinates are derived as (0.67869, 0.16060, 0.16060, 0.86180), (0.16060, 0.67869, 0.16060, 0.86180), (0.16060, 0.16060, 0.67869, 0.86180), (1/3, 1/3, 1/3, 0.41459), respectively. Through Eq. (18), $\mathbf{B}_1(\eta, \zeta)$ and $\mathbf{B}_2(\eta, \zeta)$ of the tetrahedron domain are determined. Then, the related formulations, such as the interpolation function Φ and strain-displacement transformation matrix \mathbf{B} of the tetrahedron element, can also be obtained through Eqs. (26) and (27c). Through the aforementioned steps, the stiffness matrix of the element is calculated in Eq. (28), in which the elasto-plastic constitutive matrix \mathbf{D}_{ep} can be returned by invoking the materials construction module (if nonlinear problems are considered), and n represents the number of triangular surface, i means the i^{th} integration point, then the stiffness matrix value of the sub-tetrahedron is calculated based on the above integration points, and afterwards, the overall stiffness matrix of the entire tetrahedral element is assembled in blocks according to the degrees of freedom.

$$\mathbf{K}_{ep} = \sum_{i=1}^{4n} \mathbf{B}^i(\xi, \eta, \zeta) \mathbf{D}_{ep}^i \mathbf{B}^i(\xi, \eta, \zeta) V_i \quad (28)$$

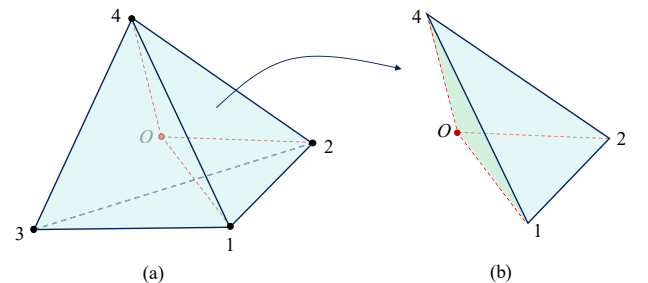
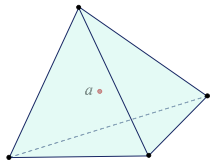
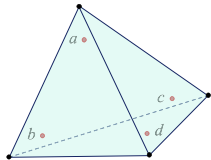


Fig. 4. Illustration of sub-tetrahedron in tetrahedron: (a) tetrahedron cell and (b) sub-tetrahedron.

Table 1
Hammer integration points in the sub-tetrahedron domain.

Accuracy	Location	Error	Points	Coordinates	Weight*
Linear		$R = O(h^2)$	a	$\frac{1}{4}, \frac{1}{4}, \frac{1}{4}, \frac{1}{4}$	1
Quadratic		$R = O(h^3)$	a b c d	$\alpha, \beta, \beta, \beta$ $\beta, \alpha, \beta, \beta$ $\beta, \beta, \alpha, \beta$ $\beta, \beta, \beta, \alpha$	$\frac{1}{4}$ $\frac{1}{4}$ $\frac{1}{4}$ $\frac{1}{4}$
			$\alpha = 0.58541020$ $\beta = 0.13819660$		

* The domain of integration in the tetrahedron is related only to the variables themselves, the sum of the weights of the integration points should equal 1/6, thus the weights listed in the table should be multiplied by 1/6.

3. Numerical example verification

The aforementioned algorithms have been integrated into the large-scale finite element analysis software GEODYNA (Zou et al., 2018), which is independently developed by the authors. And the accuracy and the universality of the proposed method for different analysis are discussed in this section. Specifically, four example simulations are investigated, including cantilever beam structure, one simply supported beam structure, and a complex metal component.

3.1. Accuracy Verification

3.1.1. Bending analysis of cantilever beam

A schematic is provided in Fig. 5, for demonstrating the geometric information, and the left end of the beam is rigidly fixed, and a concentrated force load is applied to the right end of the cantilever beam. The purpose of this simulation is to validate the rationality and accuracy of proposed method via comparing with theoretical solutions and FEM. And the linear tetrahedron is used to discretize the model, and a total of 5620 cells and 3269 nodes are generated. A completed grid model is shown in Fig. 5.

The relevant parameters are assumed as follows: The load $F = 0.1$ N is applied to the free end, the material is homogeneous and isotropic,

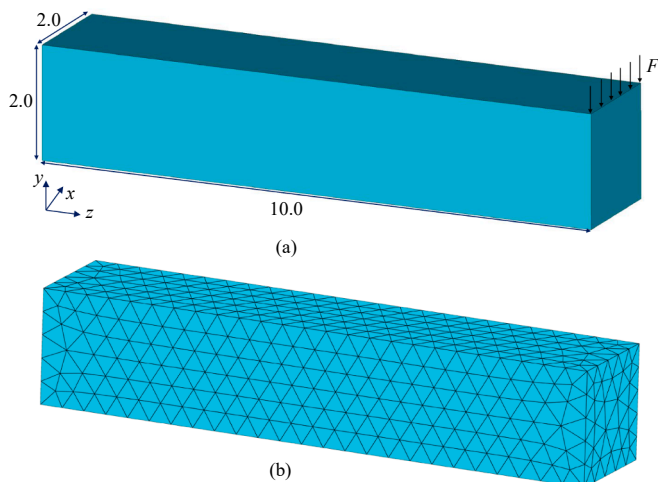


Fig. 5. Diagram of rectangular section beam: (a) geometry and (b) tetrahedron discretization.

and the elastic modulus is $E = 25$ Pa, Poisson's ratio $\nu = 0.3$ (Gain et al., 2014). The obtained displacement results of free end are given in Table 2, and the stress and deformation of the cantilever beam calculated by the proposed method is illustrated in Fig. 6. Additionally, in order to compare reasonably, the isoparametric finite element calculation results are offered in this section, and the theoretical solution has been provided in literature (Gain et al., 2014). As it can be seen, the accuracy of the proposed method is basically the same as that of the isoparametric finite element, meaning that the correctness of the proposed method is demonstrated.

3.2. Applications of mixed-order analysis

3.2.1. Element order conversion approach

The mixed order element allows the calculation with elements of different order reasonably determined according to the actual analysis needs, in this manner, the accuracy and efficiency can be improved simultaneously. In order to meet different analysis requirements, this paper provides two approaches for the order conversion, which are introduced in detail as follow.

(1) Flexural angle index

The flexural angle index θ is proposed for the conversion of mixed-order elements, whose schematic diagram is provided in Fig. 7. The detailed introduction is as follows: the simulation calculation based on the total quadratic elements is firstly performed, and then the deformations would emerge if the structure is subjected to external forces, and the flexural angle index can be determined, which is formed through vector $\vec{51}$ and vector $\vec{52}$ after deformation, and then subtract it from the 180° to obtain the flexural angle θ .

Then a threshold can be defined, once the bending angle of the edge is less than the threshold, the edge will be reduced to a linear form, thus in this way, the assignment function of different order elements representing different precision is realized.

(2) Regional customization

In addition to the above approach, the region of the first-order cells and the quadratic cells can be customized according to the demands. The schematic diagram of the principle is given in Fig. 8. For example, the area A is set as the quadratic cells, and the area C is defined as the first-order cells, then the connection area B is converted into the mixed-order cells by the self-compiled algorithm.

3.2.2. Simply supported beam

Fig. 9 shows the geometry and mesh discretization of a simply supported beam, in which 5478 quadratic cells and 3202 nodes are

Table 2
Displacements along y-direction of free-end for the cantilever beam.

Content	FEM (linear)	Presented method (linear)	FEM (quadratic)	Presented method (quadratic)	Theoretical solution
Displacement (unit: m)	0.942	0.942	1.032	1.032	1.009
Relative accuracy (%)	6.64	6.64	2.28	2.28	--

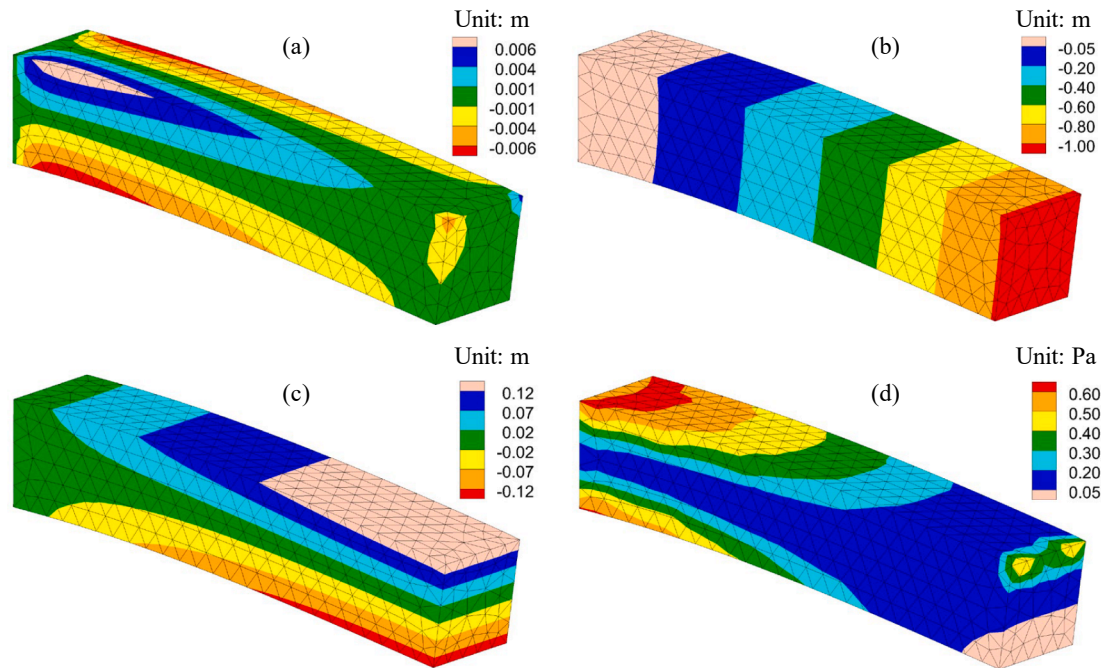


Fig. 6. Diagram of stress and deformation for cantilever beam: (a) x-direction, (b) y-direction, (c) z-direction and (d) Von-Mises stress.

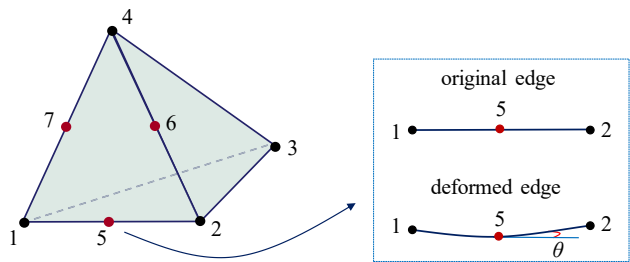


Fig. 7. Schematic diagram of flexural angle index definition.

considered, and the geometric shape and loading conditions are also shown in Fig. 9. Specifically, the elastic modulus E is equal to 3.0×10^8 Pa, Poisson's ratio μ is equal to 0.2, and the applied concentrated load F at the mid-span is equal to 9.8×10^5 N. In this section, different mixed-order schemes are considered to the calculation domain via the flexural angle index approach as shown in Table 4. And the deflection of the representative points of the top central axis (shown in Fig. 9) are observed to compare the performance of different schemes.

Table 4 shows the maximum vertical deformation results obtained through different schemes, and the comparisons of degrees of freedom are also offered. Meanwhile, the comparison of node deformation at the observation position is provided in Fig. 10. Obviously, the cross-order element can almost achieve the accuracy of quadratic isoparametric elements, while only a few degrees of freedom are required. For example, the degrees of freedom in the scheme C ($\theta = 0.2^\circ$) have been

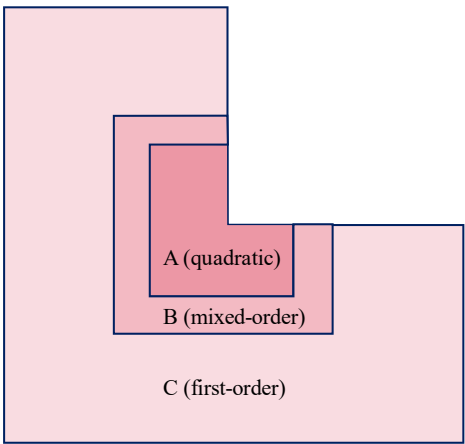


Fig. 8. Schematic diagram of the principle for regional customization.

decreased by 52.3 %, while difference in calculation accuracy is only 1.14 %, indicating the calculation accuracy can be maintained remarkably.

3.2.3. *L-component beam*

Fig. 11 shows the geometry and mesh discretization of the L-component beam, where 2619 quadratic cells and 4495 nodes are discretized, meanwhile, the geometric information and loading conditions are also depicted, where the elastic modulus $E = 3.0 \times 10^{10}$ Pa, Poisson's

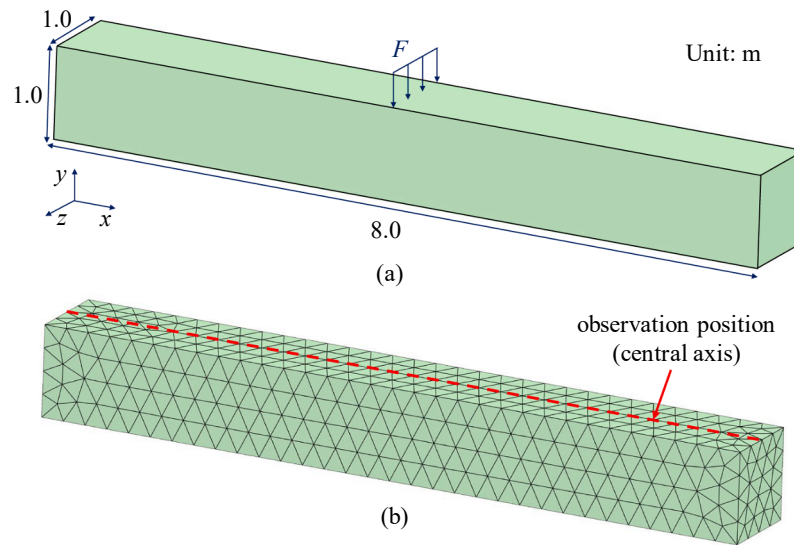


Fig. 9. Geometry description and mesh discretization of simply supported beam.

Table 4

Maximum vertical deformation of simply supported beam.

Flexural angle θ	0.0°	0.1°	0.2°	0.3°	0.4°
Dofs	5478	3544	2611	2097	1642
Dofs reduction (%)	0.0	35.30	52.33	61.72	70.03
Displacement (unit: m)	-0.463	-0.462	-0.458	-0.451	-0.442
Relative accuracy (%)	--	0.22	1.08	2.59	4.54

ratio $\mu = 0.2$. And the applied load F at the right free-end is equal to 7.2×10^5 N.

The spatial distribution of stress and deformation is shown in Figs. 12–14, meanwhile, the results generate from the representative positions, which is displayed in Fig. 11, are drawn in Figs. 15–16. As it can be seen, the results of the quadratic elements can almost be reconstructed by the regional customization, indicating that the proposed method can significantly promote the computational efficiency without affecting accuracy.

4. Conclusion

In this paper, a flexible mixed-order tetrahedrons is presented in the framework of SBFEM with the independent assortment of quadratic and first order cells, wherein the interpolation function for circumferential boundary is formulated by combining triangle area coordinates and the drawing method. Afterwards, the accuracy and applicability of the proposed approach are demonstrated by using several examples. The

main conclusions are summarized as follows:

(1) The results of bending analysis of cantilever beam align well with the theoretical solution and classical isoparametric quadratic elements, indicating the rationality of the proposed approach is validated.

(2) Compared with the quadratic elements, an enhancement of efficiency has been significantly achieved through the proposed method. The satisfactory combination of quadratic and first order cells for tetrahedrons is accomplished based on conversion index, including the angle index calculated from edges and regional customization, which makes the computing resource allocation optimized. In this manner, the calculation efficiency can be improved by more than 40 % with no significant loss of the precision.

The proposed method has the potential to be extended to hexahedrons and polyhedrons to further enhance its universality, which is also a major direction for the future research.

CRediT authorship contribution statement

Kai Chen: Writing – original draft, Software, Formal analysis. **Degao Zou:** Writing – review & editing, Software. **Guoyang Yi:** Validation, Investigation. **Xiupeng Nie:** Writing – review & editing, Formal analysis. **Yongqian Qu:** Validation, Formal analysis.

Declaration of competing interest

The authors declare that they have no known competing financial interests or personal relationships that could have appeared to influence

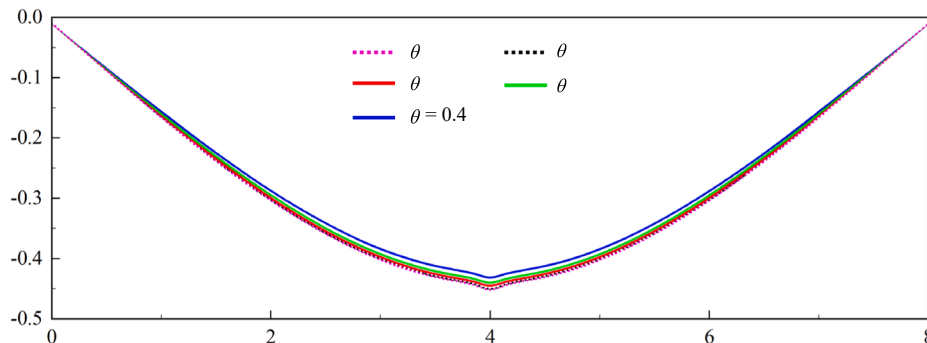


Fig. 10. Assignment for boundary line elements order of supported beam.

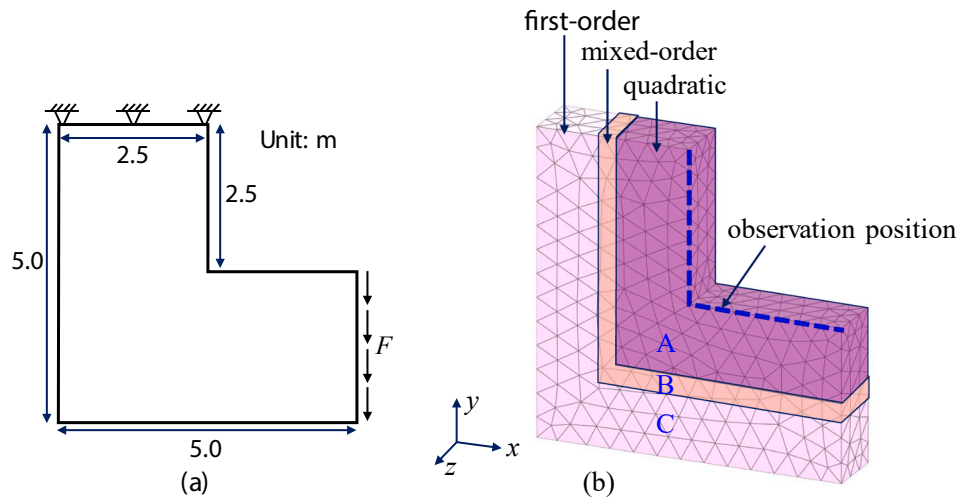


Fig. 11. Geometry information and discretization of L-component beam.

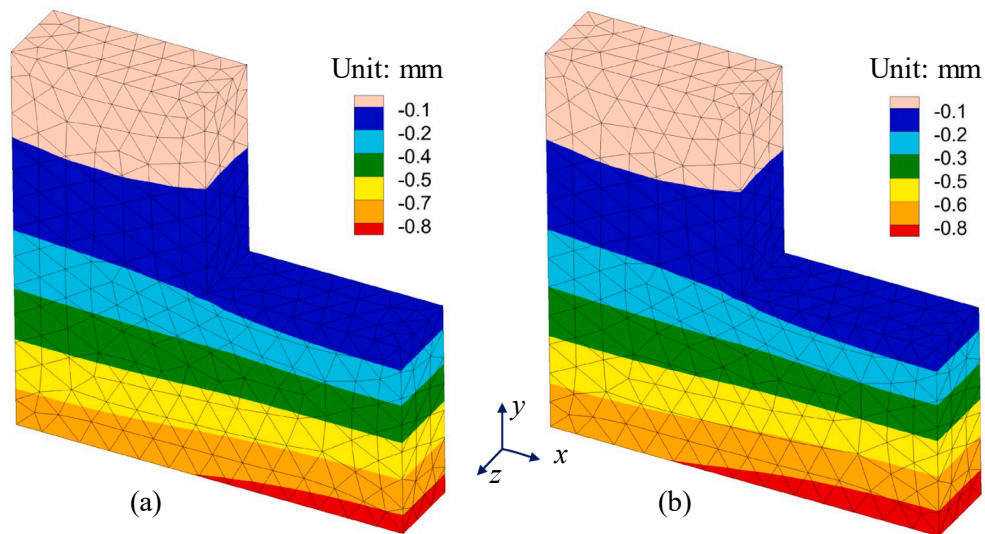


Fig. 12. Spatial distribution law of displacement along x -direction for L-component beam: (a) quadratic elements and (b) presented method.

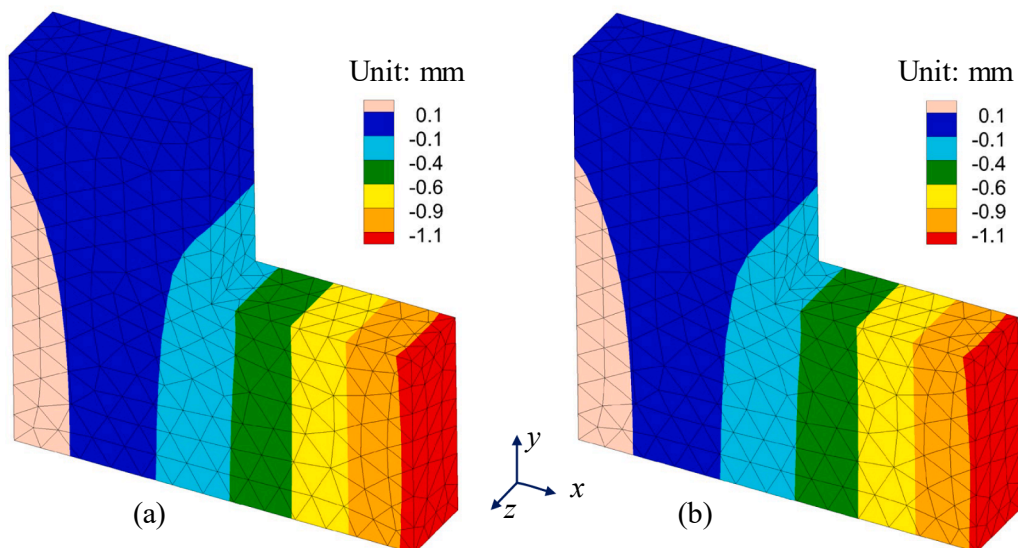


Fig. 13. Spatial distribution law of displacement along y -direction for L-component beam: (a) quadratic elements and (b) presented method.

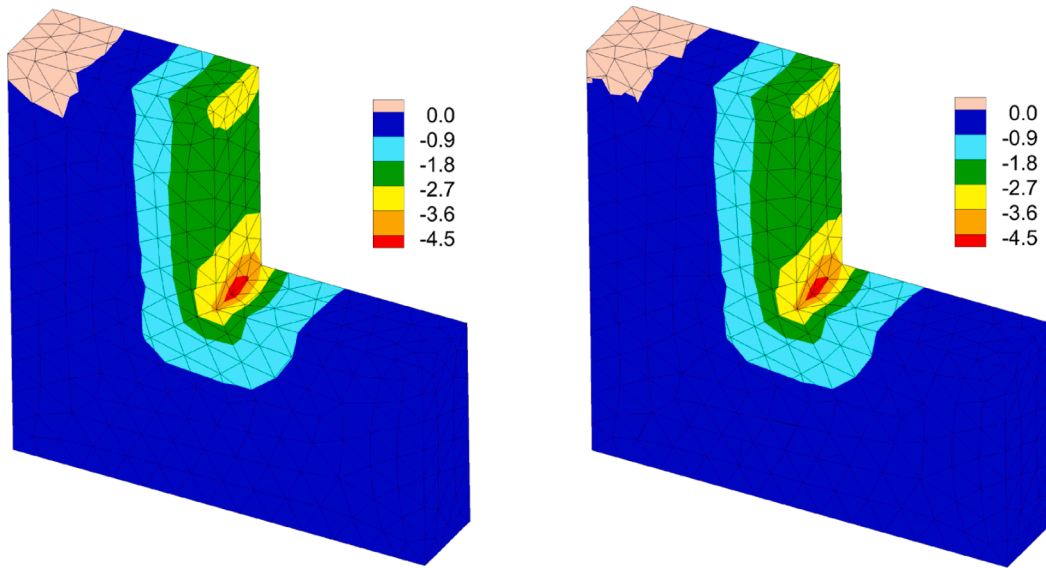


Fig. 14. Spatial distribution law of minor principal stress for L-component beam: (a) quadratic elements and (b) presented method.

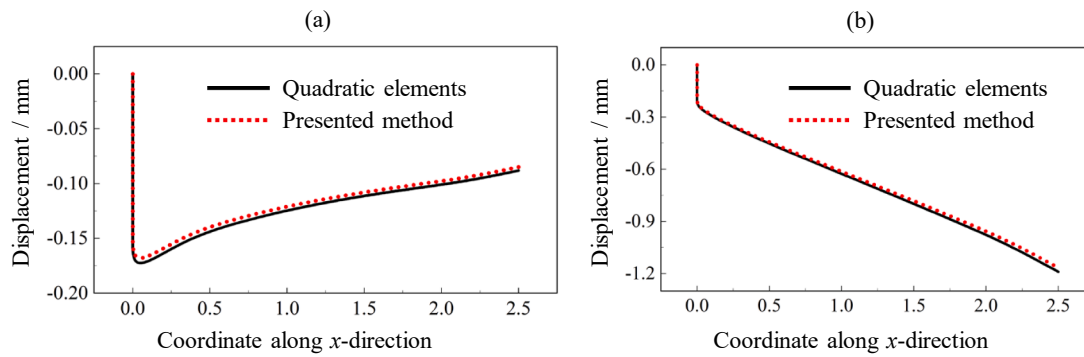


Fig. 15. Spatial distribution law of minor principal stress for L-component beam: (a) displacement along x-direction and (b) displacement along y-direction.

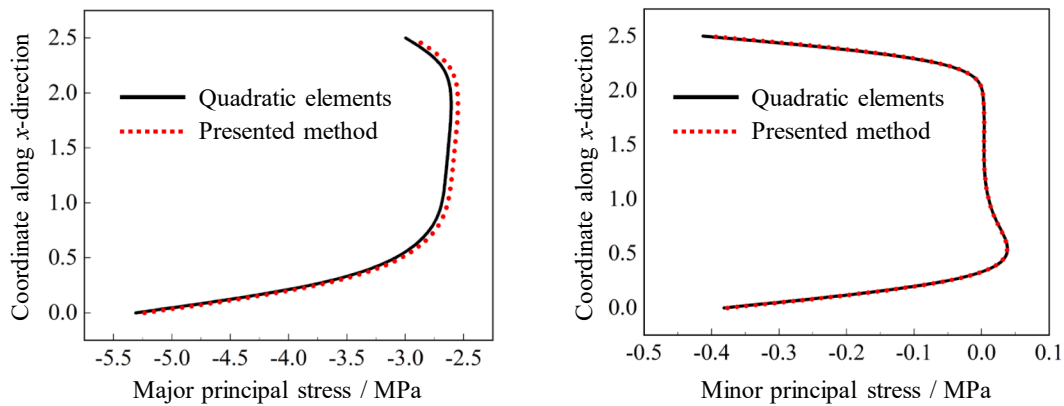


Fig. 16. Spatial distribution law of minor principal stress for L-component beam.

the work reported in this paper.

Data availability

Data will be made available on request.

Acknowledgements

This work was supported by the National Natural Science Foundation of China (Grant Nos. 52192674, 52350393, U2240211, 52109151).

References

- Areias, P., Areias, P., Areias, P., 2022. Moving least-squares in finite strain analysis with tetrahedra support. *Eng. Anal. Bound. Elem.* 139, 1–13. <https://doi.org/10.1016/j.enganabound.2022.02.010>.
- Baiges, J., Chiumenti, M., Moreira, C., Cervera, M., Codina, R., 2020. An adaptive finite element strategy for the numerical simulation of additive manufacturing processes. *Addit. Manuf.* 37, 101650. <https://doi.org/10.1016/j.addma.2020.101650>.
- Chen, K., Zou, D., Kong, X., Chan, A., Hu, Z., 2017. A novel nonlinear solution for the polygon scaled boundary finite element method and its application to geotechnical structures. *Comput. Geotech.* 82, 201–210. <https://doi.org/10.1016/j.compgeo.2016.09.013>.
- Chen, K., Zou, D., Kong, X., Yu, X., 2018. An efficient nonlinear octree SBFEM and its application to complicated geotechnical structures. *Comput. Geotech.* 96, 226–245. <https://doi.org/10.1016/j.compgeo.2017.10.021>.
- Chen, K., Zou, D., Tang, H., Liu, J., Zhuo, Y., 2021. Scaled boundary polygon formula for Cosserat continuum and its verification. *Eng. Anal. Bound. Elem.* 126, 136–150. <https://doi.org/10.1016/j.enganabound.2021.02.007>.
- Chen, K., Zou, D., Liu, J., Zhuo, Y., 2023. A high-precision formula for mixed-order polygon elements based on SBFEM. *Comput. Geotech.* 155, 105209. <https://doi.org/10.1016/j.compgeo.2022.105209>.
- Davide, M., Riccardo, Z., Enrico, N., 2021. A fully meshless approach to the numerical simulation of heat conduction problems over arbitrary 3D geometries. *Energies* 14 (5), 1351. <https://doi.org/10.3390/en14051351>.
- Du, C., Huang, W., Ghaemian, M., Jiang, S., Zhao, Z., 2023. New nonlocal multiscale damage model for modelling damage and cracking in quasi-brittle materials. *Eng. Fract. Mech.* 277, 108927. <https://doi.org/10.1016/j.engfracmech.2022.108927>.
- Gain, A., Talischi, C., Paulino, G., 2014. On the virtual element method for three-dimensional linear elasticity problems on arbitrary polyhedral meshes. *Comput. Method. Appl. M* 282, 132–160. <https://doi.org/10.1016/j.cma.2014.05.005>.
- Gao, Z., Zhao, M., Du, X., Wang, J., 2023b. Effective-mode superposition response spectrum method for three dimensional seismic response analysis of underground structures. *Soil Dynamics Earthquake Eng.* 174, 108161.
- Gao, Z., Zhao, M., Zhang, J., Du, X., Wang, J., 2023a. Effect of offset between beam outside and neutral surfaces on dynamic soil-structure interactions. *Soil Dynamics Earthquake Eng.* 168, 107806.
- Liu, J., Hao, C., Ye, W., Yang, F., Lin, G., 2021a. Free vibration and transient dynamic response of functionally graded sandwich plates with power-law nonhomogeneity by the scaled boundary finite element method. *Comput. Method. Appl. M* 376, 113665. <https://doi.org/10.1016/j.cma.2021.113665>.
- Liu, J., Hao, C., Zhou, Y., Ye, W., 2021b. Dynamic analysis of functionally graded sandwich beams using a method named scaled finite element method. *Eng. Anal. Bound. Elem.* 130, 161–175. <https://doi.org/10.1016/j.enganabound.2021.05.010>.
- Maciej, G., 2023. Simulation of processes and structures in the synapse in the context of tetrahedral mesh quality. *Comput. Math. Appl.* 145, 58–64. <https://doi.org/10.1016/j.camwa.2023.06.005>.
- Meneghetti, G., Campagnolo, A., Avallé, M., Castagnetti, D., Colussi, M., Corigliano, P., Zuccarello, B., 2018. Rapid evaluation of notch stress intensity factors using the peak stress method: comparison of commercial finite element codes for a range of mesh patterns. *Fatigue Fract. Eng.* M 41 (5), 1044–1063. <https://doi.org/10.1111/ffe.12751>.
- Nie, X., Chen, K., Zou, D., Kong, X., Liu, J., Qu, Y., 2022. Slope stability analysis based on SBFEM and multistage polytree-based refinement algorithms. *Comput. Geotech.* 149, 104861. <https://doi.org/10.1016/j.compgeo.2022.104861>.
- Nuo, L., Juan, C., Chi-Wang, S., 2022. A high order positivity-preserving conservative WENO remapping method on 3D tetrahedral meshes. *Comput. Method. Appl. M* 395, 115037. <https://doi.org/10.1016/j.cma.2022.115037>.
- Qu, Y., Zou, D., Kong, X., Yu, X., Chen, K., 2020. Seismic cracking evolution for anti-seepage face slabs in concrete faced rockfill dams based on cohesive zone model in explicit SBFEM-FEM frame. *Soil. Dyn. Earthq. Eng.* 133, 106106.1–106106.14. <https://doi.org/10.1016/j.soildyn.2020.106106>.
- Rong, Z., Liu, Y., Yin, C., Wang, L., Ma, X., Qiu, C., Zhang, B., Ren, X., Su, Y., Weng, A., 2022. Three-dimensional magnetotelluric inversion for arbitrarily anisotropic earth using unstructured tetrahedral discretization. *J. Geophys. Res.* 127 (8). <https://doi.org/10.1029/2021JB023778> e2021JB023778.
- Saputra, A., Talebi, H., Tran, D., Birk, C., Song, C., 2017. Automatic image-based stress analysis by the scaled boundary finite element method. *Int. J. Numer. Meth. Eng.* 109 (5), 697–738. <https://doi.org/10.1002/nme.5304>.
- Schneider, T., Hu, Y., Gao, X., Dumas, J., Zorin, D., Panozzo, D., 2022. A large-scale comparison of tetrahedral and hexahedral elements for solving elliptic PDEs with the finite element method. *ACM. T. Graphic* 41 (3), 1–14. <https://doi.org/10.1145/3508372>.
- Shen, X., Du, C., Jiang, S., Zhang, P., Chen, L., 2024. Multivariate uncertainty analysis of fracture problems through model order reduction accelerated SBFEM. *Appl. Math. Model.* 125, 218–240. <https://doi.org/10.1016/j.apm.2023.08.040>.
- Song, C., 2009. The scaled boundary finite element method in structural dynamics. *Int. J. Numer. Meth. Eng.* 77 (8), 1139–1171. <https://doi.org/10.1002/nme.2454>.
- Song, C., 2018. *The scaled boundary finite element method*. John Wiley & Sons Ltd, Hoboken.
- Song, C., Wolf, J.P., 1997. The scaled boundary finite-element method—alias consistent infinitesimal finite-element cell method—for elastodynamics. *Comput. Method. Appl. M* 147 (3–4), 329–355. [https://doi.org/10.1016/S0045-7825\(97\)00021-2](https://doi.org/10.1016/S0045-7825(97)00021-2).
- Sukumar, N., Tabarraei, A., 2004. Conforming polygon finite elements. *Int. J. Numer. Meth. Eng.* 61, 2045–2066. <https://doi.org/10.1002/nme.1141>.
- Utku, M., 1999. An improved transformation for universal serendipity elements. *Comput. Struct.* 73 (1–5), 199–206. [https://doi.org/10.1016/S0045-7949\(98\)00266-1](https://doi.org/10.1016/S0045-7949(98)00266-1).
- Wriggers, P., Hudobivnik, B., Aldakheel, F., 2021. NURBS-based geometries: A mapping approach for virtual serendipity elements. *Comput. Method. Appl. M* 378, 113732. <https://doi.org/10.1016/j.cma.2021.113732>.
- Ye, W., Zang, Q., Liu, J., Yang, F., Lin, G., 2023. Three-dimensional bending and free vibration analyses of laminated cylindrical panel with/without elastic foundation using two-dimensional discrete method. *Soil. Dyn. Earthq. Eng.* 168, 107831. <https://doi.org/10.1016/j.soildyn.2023.107831>.
- Yu, K., Yang, Z., Li, H., Ooi, E., Li, S., Liu, G., 2023. A mesoscale modelling approach coupling SBFEM, continuous damage phase-field model and discrete cohesive crack model for concrete fracture. *Eng. Fract. Mech.* 278, 109030. <https://doi.org/10.1016/j.engfracmech.2022.109030>.
- Zang, Q., Liu, J., Ye, W., Yang, F., Pang, R., Lin, G., 2023. High-performance bending and buckling analyses of cylindrical shells resting on elastic foundation using isogeometric scaled boundary finite element method. *Eur. J. Mech. A-Solid* 100, 105013. <https://doi.org/10.1016/j.euromechsol.2023.105013>.
- Zhang, Z., Dissanayake, D., Saputra, A., Wu, D., Song, C., 2018. Three-dimensional damage analysis by the scaled boundary finite element method. *Comput. Struct.* 206, 1–17. <https://doi.org/10.1016/j.compstruc.2018.06.008>.
- Zhang, W., Li, D., Zhang, J., Guo, X., 2016. Minimum length scale control in structural topology optimization based on the Moving Morphable Components (MMC) approach. *Comput. Method. Appl. M* 311, 327–355. <https://doi.org/10.1016/j.cma.2016.08.022>.
- Zhang, Z., Liu, Y., Dissanayake, D., Saputra, A., Song, C., 2019. Nonlocal damage modelling by the scaled boundary finite element method. *Eng. Anal. Bound. Elem.* 99, 29–45. <https://doi.org/10.1016/j.enganabound.2018.10.006>.
- Zhang, J., Zhao, M., Eisenträge, S., Du, X., Song, C., 2022. An asynchronous parallel explicit solver based on scaled boundary finite element method using octree meshes. *Comput. Method. Appl. M* 401, 115653. <https://doi.org/10.1016/j.cma.2022.115653>.
- Zhang, J., Wang, P., Zhao, M., Liu, L., Qu, X., Du, X., 2023c. A scaled boundary finite element method for soil dynamic impedance of pile groups using hybrid quadtree mesh considering horizontal vibration. *Eng. Anal. Bound. Elem.* 153, 226–241. <https://doi.org/10.1016/j.enganabound.2023.05.029>.
- Zhang, W., Xiao, Z., Liu, C., Mei, Y., Youn, S., Guo, X., 2020. A scaled boundary finite element based explicit topology optimization approach for three-dimensional structures. *Int. J. Numer. Meth. Eng.* 121 (21), 4878–4900. <https://doi.org/10.1002/nme.6498>.
- Zhang, G., Zhao, M., Zhang, J., Du, X., 2023a. scaled boundary perfectly matched layer (SBPML): a novel 3D time-domain artificial boundary method for wave problem in general-shaped and heterogeneous infinite domain. *Comput. Method. Appl. M* 403, 115738. <https://doi.org/10.1016/j.cma.2022.115738>.
- Zhang, G., Zhao, M., Du, X., Zhang, J., 2023b. Time-domain scaled boundary perfectly matched layer for elastic wave propagation. *Int. J. Numer. Meth. Eng.* 124 (18), 3906–3934. <https://doi.org/10.1002/nme.7300>.
- Zhang, G., Zhao, M., Zhang, J., Wang, J., Du, X., 2024. Scaled boundary perfectly matched layer for wave propagation in a three-dimensional poroelastic medium. *Appl. Math. Model.* 125, 108–138. <https://doi.org/10.1016/j.apm.2023.09.028>.
- Zhao, M., Liu, P., Zhang, J., Zhang, G., Gao, Z., Du, X., 2023. A direct time-domain FEM-SBFEM-SBPML method for soil-structure interaction analysis using quadtree mesh. *Comput. Geotech.* 161, 105597. <https://doi.org/10.1016/j.compgeo.2023.105597>.
- Zou, D., Liu, J., Chen, K., et al., 2018. *Theoretical Introduction and Operation Instructions of the Finite Element High Performance Analysis Software System for Large Geotechnical Engineering*. Dalian University of Technology Press, Dalian.